Journal of Porphyrins and Phthalocyanines
J. Porphyrins Phthalocyanines 2020; **24**: 662–674
DOI: 10.1142/S1088424619501190

Published at https://www.worldscinet.com/jpp/

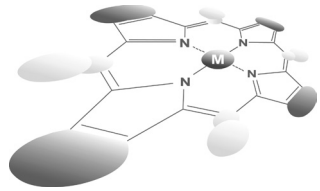

Synthesis, characterization, OFET, and DFT study of the novel ball-type metallophthalocyanines bridged with four diaminopyrimidine-dithiol

Fadime Molla[a], Ayşegül Yazıcı[a], Nursel Acar Selçuki*[b], Ahmet Altındal[c], Bekir Salih[d] and Özer Bekaroğlu*[e]

[a]*Department of Chemistry, Faculty of Science, Fırat University, Elazığ, TR-23119, Turkey*
[b]*Department of Chemistry, Faculty of Science, Ege University, Bornova, İzmir, TR-35100, Turkey*
[c]*Department of Physics, Faculty of Science and Letters, Yıldız Technical University, Esenler-Davutpaşa-Istanbul, TR-34220, Turkey*
[d]*Department of Chemistry, Faculty of Science, Hacettepe University, Beytepe, Ankara, TR-06800, Turkey*
[e]*Faculty of Pharmacy, Istinye University, Istanbul, TR-34010, Turkey*

Dedicated to Professor Roberto Paolesse on the occasion of his 60th birthday.

Received 15 May 2019
Accepted 17 August 2019

ABSTRACT: Co2Pc2 (**2**) and Zn2Pc2 (**3**) were obtained in DMF and LuPc2 (**4**) was obtained in hexanol by the cyclotetramerization of novel diphthalonitrile (**1**). Synthesized compounds were characterized by FT-IR, ^{1}H-NMR, elemental analyses, MALDI-TOF MS and UV-vis spectroscopy techniques. Optimized geometries and electronic structures for compounds **2**, **3** and **4** were investigated by Density Functional Theory (DFT) and Time Dependent Density Functional Theory (TD-DFT). In compound **2**, a new bond was observed between Co centers forming two Co(III) with the interaction of d orbitals. Computational and experimental UV-vis spectra in DMF were found in agreement for the investigated compounds. Vertical and adiabatic ionization potentials for the studied systems were also calculated. The gate dielectric performances of thin films obtained from these compounds were investigated by fabricating ITO/**2–4**/Au devices. The observed reverse bias J-V characteristics revealed that the leakage current in ITO/**2–4**/Au devices is because of the Poole–Frenkel effect. The effect of the gate dielectric on the OFET performance parameters was also investigated by fabricating bottom-gate top-contact OFET using pentacene as the active layer. Maximum field effect mobility was observed with the **2**-based OFET device. Calculated HOMO–LUMO gap, hole reorganization energy and ionization energy have also supported the experimental results which indicate that **2** is the most suitable system for OFET devices.

KEYWORDS: ball-type phthalocyanines, homodinuclear, leakage current, density functional theory, OFET.

INTRODUCTION

Phthalocyanines (Pcs) have an important place among today's products because of their possible applications in all fields of the technology [1–3]. Therefore, interest in synthesis of phthalocyanines with different properties has increased significantly for new application areas in recent years [4, 5]. These properties can be provided by connecting different groups to peripheral/nonperipheral positions and changing the central metal ions [6–8]. Ball-type phthalocyanines are a new type of phthalocyanines first reported in 2002 [9, 10].

*Correspondence to: Nursel Acar Selçuki, tel.: +90-232-3112387, fax: +90-232-3888264, email: nursel.acar@ege.edu.tr, ORCID: 0000-0001-9292-0637; Özer Bekaroğlu, tel.: +90-216-3590130, fax: +90-216-3860824, email: obek@itu.edu.tr.

In our previous work, we successfully synthesized oxygen-bridged phthalocyanine molecules starting from 5,6-diamino-2,4-dihydroxypyrimidine and investigated their OFET properties [11].

Recently, organic semiconductor materials have attracted great interest because of their potential usage in flexible electronic devices such as organic solar cells [12], organic field effect transistors (OFET) [6, 13, 14] and chemical sensors [15–18]. Many studies have concentrated on synthesis of organic semiconductors with high field effects; however, numerous work was performed on organic dielectrics [19]. Organic gate dielectrics could be useful in OFETs due to their solution processability, compatibility with flexible substrates, and tunability of physical properties. More recently, several polymeric materials such as poly(4-vinylphenol), polyimide, poly(methylmethacrylate), and polystyrene [20–22] have been used as gate dielectrics for high performance OFET fabrication. Because of poor semiconductor–dielectric interface and high leakage current in polymeric gate dielectrics, development of new gate dielectrics with improved interface and low leakage current is essential.

Our group has been devoted to research on phthalocyanine for thirty years and for the last fifteen years we have pioneered a new class "ball-type" Pcs. Though those compounds show interesting and more versatile physical and chemical properties, there is little publication about them in the literature. It is well-known that depending on the organic groups of the peripheral or nonperipheral positions of phthalocyanines, electronic properties change drastically. Therefore, changing bridged compounds with electron-donating or electron-accepting properties affects the physical and chemical properties of the ball-type phthalocyanines on a large scale. Furthermore, intermolecular distance (distance between Pc rings), π–π interaction and polarity of the molecules are important in enhancing OFET properties. Formerly, we investigated oxygen-bridged phthalocyanine molecules [11] and we extend this study by studying ball-type Pcs with S bridges, which are expected to be more flexible Pcs because of the longer C–S bonds.

In the present study, three new ball-type phthalocyanines containing four 5,6-diaminopyrimidine-2,4-dithiol bridged ligands have been synthesized and DFT/TD-DFT were performed to investigate geometrical parameters, electrostatic potentials, ionization potentials, hole reorganization energies and to compare UV-vis absorption spectra of the investigated compounds.

EXPERIMENTAL

Materials

All solvents (reagent grade) and raw materials used were supplied by Sigma–Aldrich and were directly used. An Ati Unicam Mattson 1000 Series FT-IR spectrometer (KBr pellets) was used to record the IR spectra. A Shimadzu UV-1700 spectrometer was used to record UV-vis spectra. LECO CHNS 932 was used to perform the elemental analyses. ^{1}H-NMR spectra were measured at 400 MHz on a Bruker 400 spectrometer at room temperature using tetramethylsilane (TMS) as the internal standard. Mass spectra were recorded on a Voyager-DE™ PRO MALDI-TOF mass spectrometer (Applied Biosystems, USA) arranged with a nitrogen UV-Laser operating at 337 nm either in MALDI or LDI modes. Spectra were recorded in positive ion and linear modes between 50–100 laser shots.

Synthesis

***Synthesis of* [4,4′-(5,6-*diaminopyrimidine*-2,4-*diyl*) *bis*(*tiyo*)]*diphthalonitrile* (1).** Dry DMF (10 ml) was taken in a reaction flask and Ar gas was passed through for about 15 min. Then 4-nitrophthalonitrile (1.731 g, 10 mmol) and 5,6-diaminopyrimidine-2,4-dithiol (0.871 g, 5 mmol) were added to the solvent medium. After the reaction mixture was stirred at 70 °C for 30 min, the powdery anhydrous K_2CO_3 (2 g, 14.5 mmol) was added to the reaction mixture under effective stirring in equal portions in 3 h and at same temperature. The reaction lasted 96 h under these conditions. The reaction mixture was then cooled to room temperature and was precipitated by adding dropwise to the ice water mixture. The precipitate was filtered off and washed several times with hot water, chloroform, and dimethyl ether. The resulting product was purified using the difference in solubility, and dried at room temperature. The pale yellow solid dissolved completely in DMF, DMSO, ethylene diamine and partly in acetone. Yield: 0.956 g (44%). Mp 172 °C. Anal. Calcd. for $C_{20}H_{10}N_8S_2$: C, 56.33; H, 2.37; N, 26.26; S,15.04%; Found : C, 56.10; H, 2.25; N, 26.92; S,15.20%. IR (KBr): υ (cm^{-1}) 3440–3359, 3095, 2928, 2233, 1657, 1579, 1385, 1262, 1097, 990. ^{1}H-NMR (400 MHz, DMSO-d_6): δ, ppm; 8.31 (2H, s), 8.19 (2H, d, J = 8.4 Hz), 7.92 (2H, d, J = 8.4 Hz), 5.77 (2H, s), 5.73 (2H, s). MS (MALDI-TOF) m/z: 427.2 $[M + H]^+$.

***Synthesis of* [2′, 10′, 16′, 24′-*tetrakis*{4,4′-(5,6-*diaminopyrimidin*-2,4-*diyl*)*bis*(*thio*)}]*diphthalocyaninato-dicobalt*(*II*) (2).** A mixture of **1** (0.055 g, 0.13 mmol) and cobalt(II) acetate (0.016 g, 0.065 mmol) with a 2:1 ratio were dissolved in 8 mL of dry DMF, and 0.2 mL of 1,5-diazabicyclo[4.3.0]non-5-ene (DBN) was added to the media. Then the reaction mixture was refluxed at 170 °C for 18 h under argon atmosphere in a sealed glass tube with continuous stirring. Afterwards, the reaction mixture was precipitated by adding dropwise to the ice water mixture at room temperature. After filtration, the unreacted starting materials were removed by washing with hot water, chloroform, ethyl acetate and methyl acetate. The green-colored product was dried at room temperature. The dark green product dissolved completely

in DMF and DMSO but dissolved only slightly in THF. Yield: 0.034 g (14%). Mp >300 °C. Anal. Calcd. for $C_{80}H_{40}N_{32}S_8Co_2$: C, 52.69; H, 2.22; N, 24.57; S, 14.06%; Found: C, 52.98; H, 2.42; N, 24.87; S, 14.55%. IR (KBr): υ (cm^{-1}) 3310–3181, 3061, 2945, 1651, 1440, 1378, 1306, 1282, 1103, 967. UV-vis (DMF), λ_{max}, nm (log ε): 690 (4.00), 619 (3.58), 345 (4.51). ^{1}H-NMR (DMSO-d_6): δ, ppm 8.15–7.67 (24H, m, Ar-H), 7.29–7.03 (16H, NH). MS (MALDI-TOF-MS) m/z: 1824.3 $[M + H]^+$.

***Synthesis of* [2′, 10′, 16′, 24′-*tetrakis*{4,4′-(5,6-*diaminopyrimidin*-2,4-*diyl*)*bis*(*thio*)}]*diphthalocyaninatodizinc*(*II*) (3).** Compound **3** was synthesized in a similar manner to that described above for **2**, using zinc acetate (0.014 g, 0.065 mmol). Yield: 0.032 g (13%). Mp >300 °C. Anal. Calcd. for $C_{80}H_{40}N_{32}S_8Zn_2$: C, 52.32; H, 2.20; N, 24.40; S, 13.97%; Found: C, 52.93; H, 2.33; N, 24.92; S, 14.15%. IR (KBr): υ (cm^{-1}) 3334–3272, 3042, 2902; 1592, 1428, 1314, 1204, 1159, 1107, 1030, 991. UV-vis (DMF), λ_{max}, nm (log ε): 685 (4.58), 617 (3.92), 330 (4.55). ^{1}H-NMR (DMSO-d_6): δ, ppm 8.20–7.74 (24H, m, Ar-H), 7.27–6.99 (16H, NH). MS (MALDI-TOF-MS) m/z: 1836.8 $[M + H]^+$.

***Synthesis of* [2′, 10′, 16′, 24′-*tetrakis*{4,4′-(5,6-*diaminopyrimidin*-2,4-*diyl*)*bis*(*thio*)}]*diphthalocyaninatolutetium*(*III*) (4).** A homogeneous-powdered mixture of **1** (0.046 g, 0.13 mmol) and lutetium(III)acetate (0.011 g, 0.0325 mmol) in 4:1 ratio was refluxed in hexanol in a sealed glass tube in the presence of 1,5-diazabicyclo[4.3.0]non-5-ene (DBN), under argon atmosphere at 170 °C for 18 h. The reaction mixture was precipitated in hexane (50 mL) after cooling down to room temperature. The product was purified by washing with water, ethanol and chloroform after filtration. The dark green compound dissolved completely in DMSO and DMF. Yield: 0.035 gr (14%). Mp >300 °C. Anal. Calcd. for $C_{80}H_{40}N_{32}S_8Lu$: C, 51.05; H, 2.13; N, 23.82; S, 13.61%; Found: C, 51.23; H, 2.42; N, 23.95; S;14.05%. IR (KBr): υ (cm^{-1}) 3359–3100, 2950, 1638, 1362, 1308, 1147, 1075, 842. UV-vis (DMF), λ_{max}, nm (log ε): 690 (3.52), 621 (2.97), 330 (4.07). ^{1}H-NMR (DMSO-d_6): δ, ppm 8.48–7.90 (24H, m, Ar-H), 7.36–7.10 (16H, NH). MS (MALDI-TOF-MS) m/z: 1881.5 $[M + H]^+$.

MALDI sample preparation. The mass spectrum of compound **1** was obtained without matrix. Only a 10 mg/mL sample solution in water was prepared. 1% trifluoroacetic acid was added into the sample solution and 1 µL sample solution was applied onto the silicon wafer and the mass spectrum was carried out using 50 laser shots in Laser Desorption Ionization (LDI) mode as described in our previous study [23].

For the all other complexes, MALDI matrix, 2,5-dihydroxybenzoic acid was prepared in H_2O-ACN-DMSO (45:45:10, v/v/v) containing 0.2% trifluoroacetic acid at a concentration of 10 mg/mL. The MALDI sample was prepared by mixing sample solutions (5 mg/mL in H_2O-ACN-DMSO (45:45:10, v/v/v) having 0.2% trifluoroacetic acid) with the matrix solution (1:10, v/v) in a 0.5 mL Eppendorf® micro tube. Finally 1.0 µL of this mixture was accumulated on the sample plate, dried at room temperature and then analyzed.

OFET fabrication and characterization

OFET devices were fabricated on indium tin oxide (ITO)-coated glass slides with a bottom-gate and top-contact configuration. Spin-coated thin films of the compounds **2–4** were used as the gate dielectric layer, while pentacene was used as the active layer. Before the deposition of the gate dielectric layer, ITO substrates were washed by ultrasonic treatment in isopropyl alcohol, acetone, de-ionized water and finally dried with dry nitrogen gas. Dimethylformamide solution of the compounds with a concentration of 5×10^{-3} M was spun onto the ITO surface at 1500 rpm for 80 s and then thermally treated at 120 °C for 30 min. In order to investigate the interface between the ITO substrate and the compounds, a film of gold (Au) on the Pc films with a thickness of 150 nm was formed by thermal evaporation of pure Au metal. For the fabrication of the OFET devices, a thin layer of pentacene was deposited on the gate dielectric by the thermal evaporation method. Finally, the Au source and 150 nm thick-drain electrodes were deposited by thermal evaporation through a metal shadow mask with a channel width (W) of 4 mm and a channel length (L) of 100 µm. The OFET electrical characteristics were measured using a Keithley 2400 source meter and Keithley 617 programmable electrometer under ambient conditions.

RESULTS AND DISCUSSION

Synthesis and characterization of compounds

Compound **1** is the starting material which can be synthesized *via* a single-step reaction of 5,6-diamino-pyrimidine-2,4-dithiol and 4-nitrophthalonitrile (1:2) with a yield of 44%. In the second stage of our work, **2**, **3** and **4**, which are the ball-type phthalocyanines, were synthesized by heating [4,4′-(5,6-diaminopyrimidine-2,4-diyl)-bis(thio)]diphtalonitrile **1** with $Co(OAc)_2 \cdot 4H_2O$, $Zn(OAc)_2 \cdot 2H_2O$ and $Lu(OAc)_3 \cdot H_2O$ in a sealed glass tube in the presence of 1,5-diazabicyclo[4.3.0]non-5-ene (DBN), under argon atmosphere. DMF was chosen for **2** and **3**, and hexanol was chosen for **4** as high boiling solvents in these reactions. Scheme 1 summarizes the synthesis routes and conditions for compounds **1**, **2**, **3** and **4**.

All new compounds were successfully characterized using elemental analyses, UV-vis (Fig. 1), FT-IR, ^{1}H-NMR (Fig. S1) and MALDI-TOF mass (Figs 2–5) techniques. Melting points of synthesized ball-type phthalocyanines were determined to be over 300 °C.

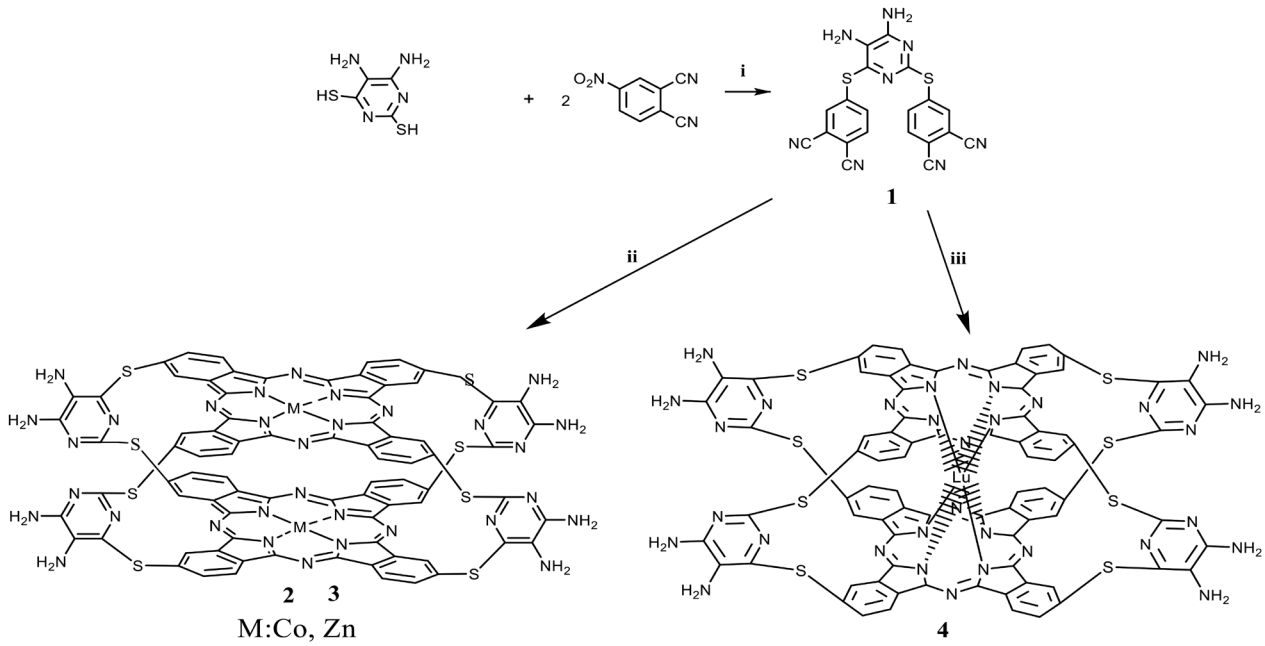

Scheme 1. Synthesis paths. (i) K_2CO_3, DMF, 96 h, 70 °C; (ii) DMF, DBN, $Co(OAc)_2 \cdot 4H_2O$ for **2**, and $Zn(OAc)_2 \cdot 2H_2O$ for **3**; (iii). Hexanol, DBN, $Lu(OAc)_3 \cdot H_2O$ for **4**

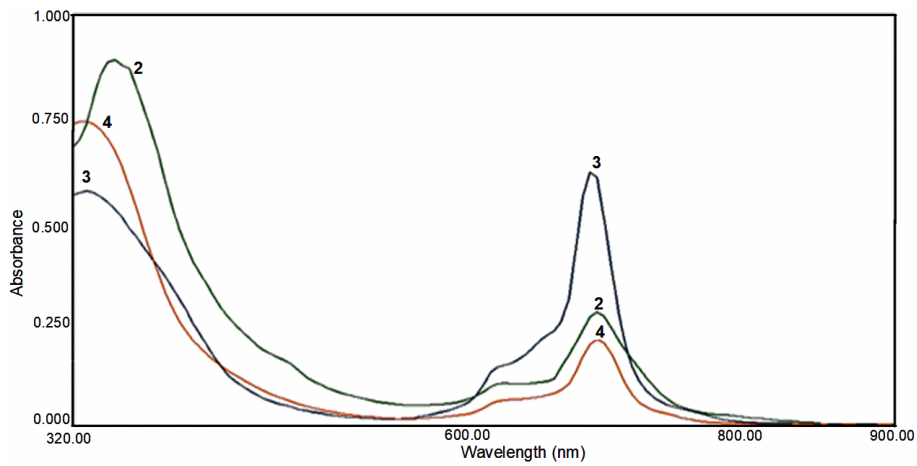

Fig. 1. UV-vis spectrum of **2** (2.74×10^{-5} M), **3** (1.63×10^{-5} M) and **4** (6.37×10^{-5} M) in DMF

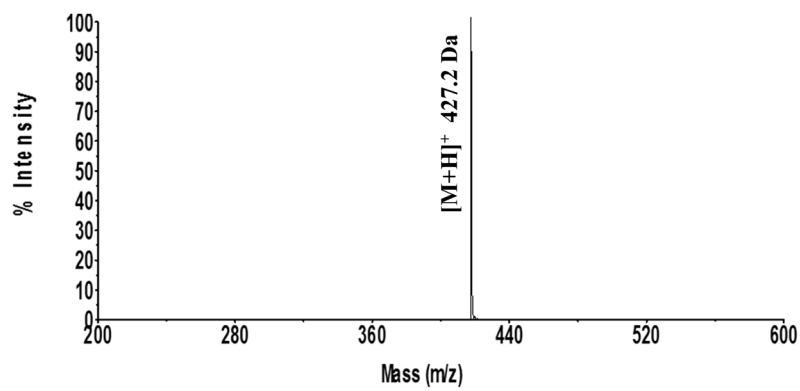

Fig. 2. Positive ion and linear mode LDI mass spectrum of **1** was obtained on silicon wafer after acidified 10 mg/mL sample solution in water by trifluoroacetic acid (1%) using nitrogen laser (at 337 nm wavelength) accumulating 50 laser shots

Q band absorptions are observed at 690, 685 and 690 nm in the electronic spectra for **2**, **3** and **4** in DMF, respectively. These bands belong to the $\pi \rightarrow \pi^*$ transitions from the highest occupied molecular orbital (HOMO) to the lowest unoccupied molecular orbital (LUMO) of the phthalocyanine ring. The Q band of **3** is broader than that of **2** and **4**. But **2** and **4** have more intense B bands than the Q bands of phthalocyanine complexes which reveal aggregation [24]. This is a result of the mixing of B bands with the charge transfer bands of the phthalocyanine complexes. The B bands for **2**, **3** and **4** were observed at 345, 330 and 330 nm in the UV region because of the transitions from lower π levels to LUMO.

Molecular structures of synthesized compounds were also supported by the results from the ^{1}H-NMR spectra. The aromatic protons of **1** appeared at 8.31 ppm (s), 8.31 ppm (d) and 7.92 ppm (d) in the ^{1}H-NMR spectrum (taken in DMSO-d_6). The NH_2 protons of compound **1** appeared as two singlets at 5.77 ppm and 5.73 ppm, which disappeared after deuterium exchange on addition of D_2O. The ^{1}H-NMR spectrum of **2** is given in Fig. S1. The ^{1}H-NMR spectra of **2**, **3** and **4** were similar to each other. In the ^{1}H-NMR spectra of compounds **2**, **3** and **4**, aromatic protons appear as broad multiplets at 8.15–7.67, 8.20–7.74 and 8.48–7.90 ppm, respectively. The NH_2 protons in compounds **2**, **3** and **4** were observed at 7.29–7.03, 7.27–6.99 and 7.36–7.10 ppm, respectively which disappeared after deuterium exchange on addition of D_2O. These peaks in compounds **2**, **3** and **4** correspond to the 16 protons belonging to the NH_2 in the structure.

The IR spectrum of compound **1** includes the NH_2 stretching bands at 3440 and 3359 cm^{-1}. Additionally, an intense stretching band at 2232 cm^{-1} showed the presence of a C≡N group in **1**. This nitrile peak observed at 2232 cm^{-1} was not observed in the IR spectrum of compounds **2**, **3** and **4**. Stretching modes at around 3360–3100 cm^{-1} belong to the -NH_2 groups in compounds **2**–**4**. Weak bands in the 3061–2902 cm^{-1} region are caused by the aromatic C–H stretches on the Pc rings.

The positive ion and linear mode MALDI-MS spectrum of compound **1** was carried out and is given in Fig. 2. Here only protonated molecular ion was observed without any impurities and fragmentations.

The positive ion and linear mode MALDI-TOF-MS spectra of cobalt, zinc and lutetium complexes were obtained and are given in Figs 3–5. Up to about 700 Da mass, all the signals resulted with MALDI matrix clusters. 2,5-dihydroxybenzoic acid MALDI matrix

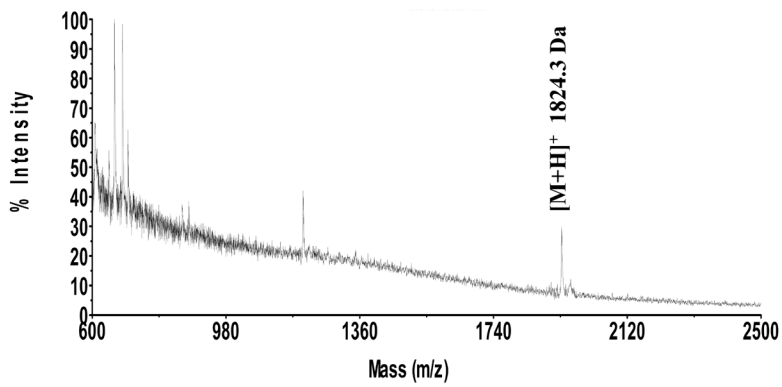

Fig. 3. Positive ion and linear mode MALDI mass spectrum of cobalt complex **2** was obtained in 2,5-dihydroxybenzoic acid MALDI matrix using nitrogen laser (at 337 nm wavelength) accumulating 100 laser shots

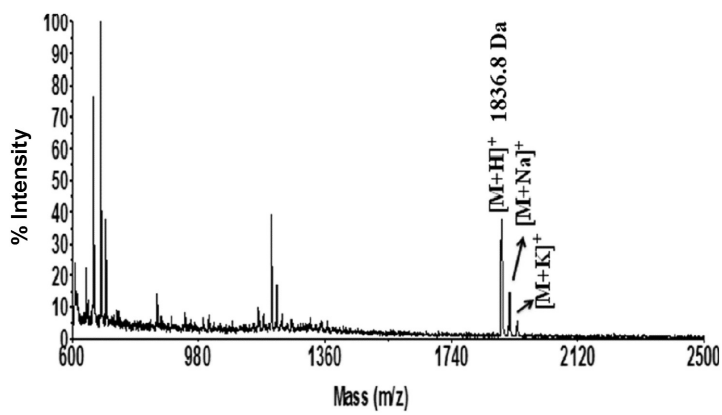

Fig. 4. Positive ion and linear mode MALDI mass spectrum of zinc complex **3** was obtained in 2,5-dihydroxybenzoic acid MALDI matrix using nitrogen laser (at 337 nm wavelength) accumulating 100 laser shots

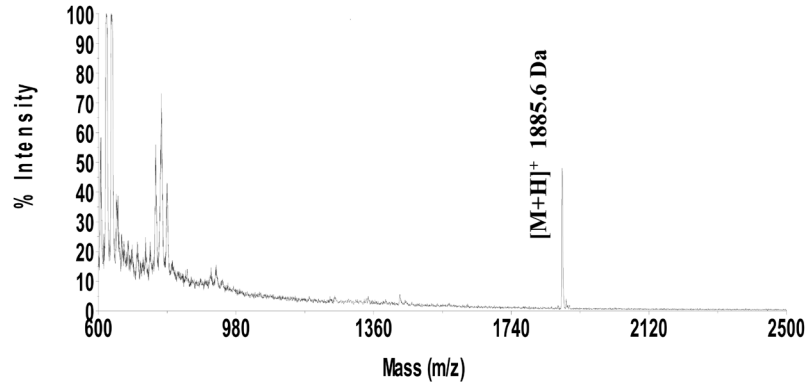

Fig. 5. Positive ion and linear mode MALDI mass spectrum of lutetium complex **4** was obtained in 2,5-dihydroxybenzoic acid MALDI matrix using nitrogen laser (at 337 nm wavelength) accumulating 100 laser shots

mainly yielded intense protonated ion signals and limited fragmentations under the MALDI-TOF-MS conditions used for these compounds except for one intense signal observed at 1180–1250 containing one metal core stable ion resulting from fragmentation of the complexes for cobalt and zinc ([M–$C_{32}H_{13}N_8S_2Co$]:1192 Da for cobalt and [$C_{32}H_{13}N_8S_2Zn$]:1198 Da for zinc complex). This was not the case for the lutetium complex which has different coordination compared to the other transition metal complexes. For the lutetium complex, the fragment ions were found to be $C_{32}H_{13}N_8Lu$:782 Da and its single- and double-sodiated adducts. All of these fragmentations occurred because of the stretched and high-energy structure of all complexes. However, any reasonable signal obtained in reflectron mode for these complexes may be attributed to the short lifetime and lower stability of the complexes under the reflectron mode conditions. Protonated ion masses of metal complexes were in good correlation with the molecular masses of the complexes. These results confirm that the metal complexes were synthesized by the correct routes in the proposed structures and the other signals resulted from fragmentation of the complexes, not from impurities.

Computational studies

Optimizations of the studied systems were carried out by Gaussian09 [25] in gas phase and in *N*,*N*-dimethyl-formamide (DMF). Molecular structures, UV-vis spectra and orbitals were visualized by Gaussview 5.0 [26]. Geometries were optimized with DFT [27] at ground state. The hybrid B3LYP functional (B3: Becke's three-parameter nonlocal exchange functional [28, 29] and LYP: Lee-Yang-Parr's correlation function [30] were used for DFT and CAM-B3LYP (Coulomb-attenuating method-B3LYP with long-range corrections) [31] was used for TD-DFT together with the 6-31G(*d*,*p*) basis set and the SDD basis set [32] (only for metals). True minimum natures of the optimized structures were verified with all positive frequencies. Calculations for excited state properties were performed using the first 100 singlet excited states for the investigated systems. Molecular orbital energies and UV-vis spectra were determined using ground-state geometries. SCF density was used to calculate the total electron density surface of the molecules both in the gas phase and in DMF. Solvent effects were investigated using the Polarizable Continuum Model (PCM) [33, 34] in ground state as implemented in Gaussian09. Natural bond orbital (NBO) [35] analysis was also performed to support the interaction of dz^2 orbitals of Co for compound **2**.

The optimized structures of **2, 3** and **4** in ground state are given in Fig. 6 in gas phase and in DMF at B3LYP/6-31G(*d*,*p*) level with SDD basis set on metals. Fig. S2 also shows molecular structures with different views of the investigated molecules in DMF. Total electronic energies including zero-point energy corrections (E_{elec} + ZPE, Hartree) and dipole moments (μ, Debye) of studied molecules calculated with B3LYP functionals using the 6-31G(*d*,*p*) basis set in the gas phase and in DMF (SDD basis set is used for metals) are given in Table S1.

Some important interatomic distances and some selected angles are given in Table 1. In order to observe and compare the changes caused by the replacement of S with O in compound **3**, C–O distances, C–O–C and O–Zn–O angles are given for gas phase in Fig. S3. The C–O distance is calculated as 1.40 Å compared to the C–S distance of 1.79 Å. Calculations reveal a wider C–O–C angle (119°) compared to the C–S–C angle (104°). Replacement of O with S increases C–X bond lengths and decreases C–X–C angles, enabling more flexibility for the molecule and thus allowing distortions from the planar Pc structure. This loss of planarity caused stronger interactions between metal centers observed in the form of shorter metal–metal distances. Planarity of the Pc can be observed using the X–Zn–X angles. The calculated O–Zn–O angle is 176° compared to the S–Zn–S angle of 169°. The same results were observed for other investigated S-bridged compounds; thus, the Pcs are not planar and are not parallel to each other (Fig. 6). For

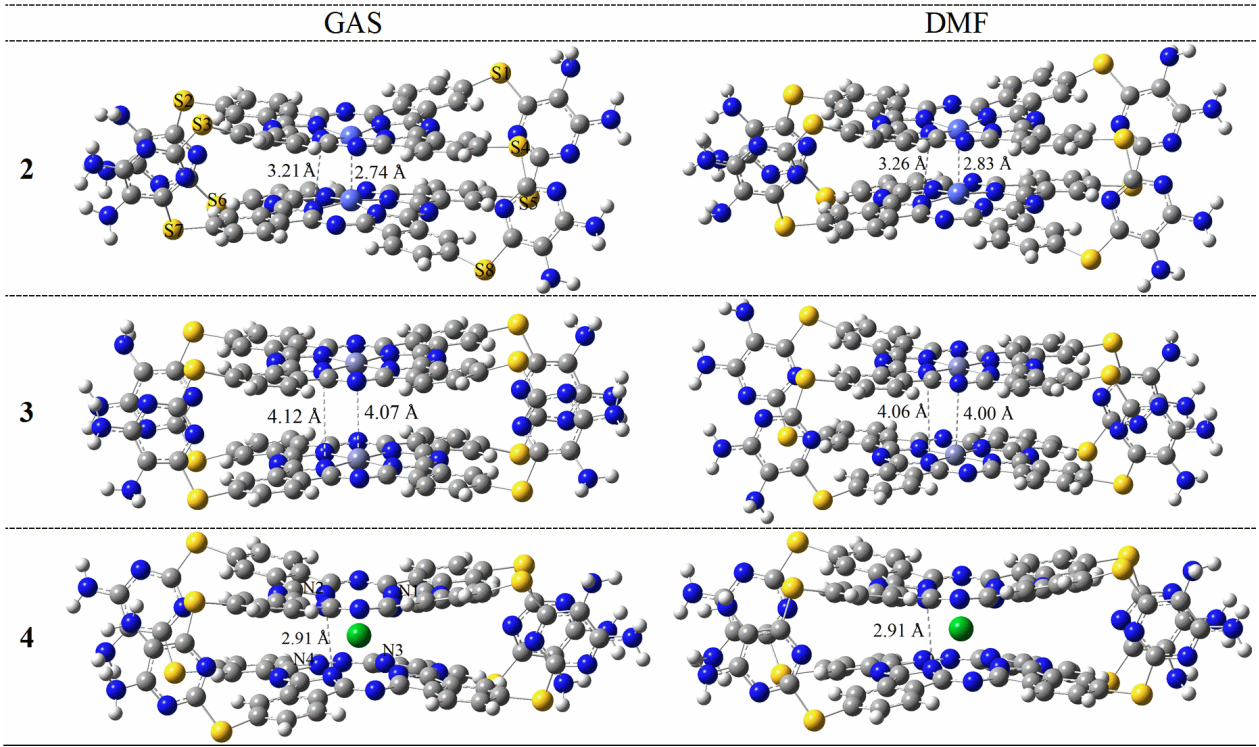

Fig. 6. Optimized geometries of **2**, **3** and **4** at B3LYP/6-31G(*d*,*p*) level with SDD basis set for metals in gas phase and in DMF

example, the deviation from the Pc planarity in compound **2** is 23° compared to 10° observed for compound **3** in gas phase. When input and output geometries were compared in gas phase, the Co–Co distance decreased from 4 Å to 2.74 Å and the square planar structure changed to a pyramidal square structure (Fig. S4).

Calculated M–M distances which are measured as 2.83 Å and 4.00 Å for **2** and **3** in DMF, respectively, revealed another important observation. In compound **2**, low spin Co(II) metals are close to each other which results overlapping of Co(II)–Co(II) orbitals (dz^2) and may lead to the formation of new orbitals (spin–spin coupling) to Co(III)–Co(III) (Fig. S5). Results obtained from ^{1}H-NMR spectra of **2** support this observation. S–S distances in the bridging diaminopyrimidine-2,4-bisthiol groups are similar in both studied media resembling the distances in **4**. Structural differences in molecules **2** and **3** are mostly caused by the different natures of the metal ions.

LUMO and HOMO energies are generally correlated with electron affinity and ionization potential, respectively. Fig. S6 displays the transition energies for HOMO–LUMO calculated for the investigated molecules in DMF. HOMO–LUMO orbital energies and energy gaps, ΔE_{H-L} are also displayed. Since Lu(III) has an unoccupied single electron, the single occupied molecular orbital (SOMO) was shown for **4**. All HOMO and LUMO energies have very small negative values in DMF at B3LYP/6-31G(*d*,*p*) and SDD (on metals) level for all investigated systems. Intramolecular charge transfer occurs much more easily with lower energy gaps. Conjugated rings on **3** and **4** act as hosts for HOMO and LUMO. LUMO is located on Co of compound **2**. The energy gap of **2** is the smallest value among the molecules in DMF. Compound **3** has the highest HOMO–LUMO energy gap with a value of 2.00 eV in DMF. Thus, **2** makes an easier charge transfer and is a better candidate than the other investigated molecules for charge transfer systems.

The absorption wavelengths and excitation energies of all investigated systems from S_0 to S_{100} states were calculated using TD-DFT at B3LYP/6-31G(*d*,*p*) and CAM-B3LYP/6-31G(*d*,*p*) levels using optimized ground-state geometries. The CAM-B3LYP values agree better with the experiments in DMF (Fig. S7); thus, CAM-B3LYP/6-31G(*d*,*p*) results are used for discussion unless otherwise stated. As an example, Q bands can be compared for compound **3**. The Q band is calculated as 690 nm with CAM-B3LYP and 666 nm with B3LYP, which deviates from the experimental value (685 nm, Fig. 1) by 5 and 19 nm, respectively.

Selected electronic transitions for **2**, **3** and **4** were displayed in Tables S2, S3 and S4, respectively. Molecular orbitals involved in electronic transitions for each compound are given in Figs S8–S10. Calculations showed that compounds **2** and **4** have transitions at a near-IR region. Thus, the following discussion is based on a UV region which started at $S_0 \rightarrow S_7$ transition (798 nm

Table 1. Important distances and angles for **2**, **3** and **4** in gas phase and in DMF, calculated at B3LYP/6-31G(*d*,*p*) level with SDD basis set for metals. (M: metal; d: distance; S–M–S and C–S–C°: angles)

	2		**3**		**4**	
	GAS	DMF	GAS	DMF	GAS	DMF
d (M···M) Å	2.74	2.83	4.00	4.02	2.45[a]	2.45[a]
d (C–S) Å	1.79	1.80	1.79	1.79	1.79	1.79
d (S1···S5) Å	5.44	5.44	5.45	5.46	5.46	5.46
d (S4···S8) Å	5.44	5.43	5.45	5.45	5.45	5.46
d (S2···S6) Å	5.44	5.44	5.45	5.46	5.46	5.46
d (S3···S7) Å	5.44	5.44	5.45	5.45	5.46	5.46
N–N[b] Å	3.20	3.26	4.12	4.06	2.91	2.91
(C–S–C)°	102	103	104	104	106	104
(S1–M–S3)°	157	158	170	177	168[c1]	166[c1]
(S2–M–S4)°	172	172	169	166	155[c2]	156[c2]
(S5–M–S7)°	172	172	169	167	156[c3]	157[c3]
(S6–M–S8)°	157	159	170	178	169[c4]	167[c4]

[a]d(N1···Lu); [b]*N–N* distance between core of Pcs; [c]1: (S1N1S3)°, c2: (S2N2S4)°, c3: (S5N3S7)°, c4: (S6N4S8)°

in DMF) for **2** and at $S_0 \rightarrow S_6$ transition (731 nm in DMF) for **4**. The $S_0 \rightarrow S_7$ transition for compound **2** has a π→π* character between HOMO and LUMO+1 orbitals at the CAM-B3LYP/6-31G(*d*,*p*) level and SDD for Co. The $S_0 \rightarrow S_9$ transition (684 nm) also has local excitation of phthalocyanine ring (LE, π→π* character) with high oscillator strength. Q bands are observed between 798 nm and 547 nm; however, *d–d* transition (LE2) and ligand-to-metal charge transfer (LMCT1: charge transfer from Pc to Co) are observed at 562 nm as well. Full metal-to-ligand charge transfer (MLCT) with a low oscillator strength between HOMO-6 and LUMO+2 orbitals is observed at 444 nm (Fig. 7 and Table S2). Between 448 nm and 396 nm, charge transfer from diaminopyrimidine to Co between HOMO-2 and LUMO (LMCT2) is observed in addition to MLCT. Except for metal–ligand interactions, intramolecular charge transfers from bridge to Pc take place (ICT2: charge transfer from S to Pc; ICT3: charge transfer from diaminopyrimidine to Pc). Those transitions with high oscillator strengths (between 357 nm and 316 nm) increase the intensities of the B bands.

Q bands for **3** are at 714 nm and 701 nm with high oscillator strengths between HOMO-1-LUMO and HOMO–LUMO orbitals and continue with different oscillator strengths up to 568 nm (Table S3 and Fig. S9). Intramolecular charge transfer from diaminopyrimidine (ligand) and S to Pc occurs between 305 nm and 353 nm. Unlike compound **2**, charge transfer between Pcs (ICT4 and ICT5) was observed due to shorter distances between Pcs. MLCT was found at 349 nm and 353 nm between HOMO-21/22/23 to LUMO+1/2/3.

Because of the odd number of total electrons for Lu(III), SOMOs (single occupied molecular orbitals) were shown with α-spin in electronic transitions (Table S4 and Fig. S10). Since 100 singlet states were insufficient to obtain the electronic transitions in LuPc, 150 singlet states were calculated for this system. Q bands for **4** are at 731 nm and 714 nm with high

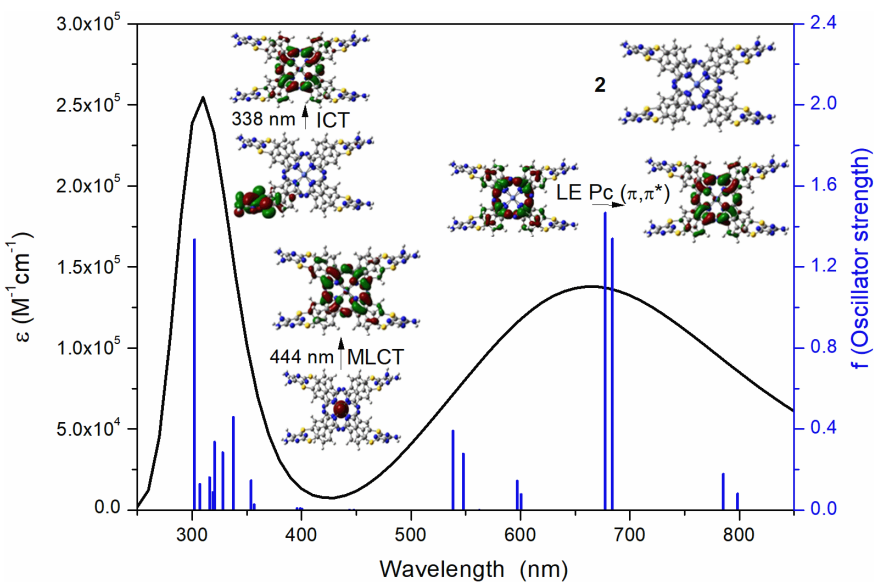

Fig. 7. UV-vis absorption spectra of **2** (with oscillator strength values) in DMF calculated at CAM-B3LYP/6-31G(*d*,*p*) and SDD (for Co) level

oscillator strengths between SOMO-1-LUMO and SOMO-LUMO+3 orbitals. Charge transfer from ligand and S to Pc was between 310 nm and 465 nm. MLCT peak was first observed at 406 nm with locally excited Pc between SOMO-33 and LUMO. At this wavelength, the intensity of the peak was also high due to the locally excited Pc (LE Pc). Since the LE Pc peaks at 400 nm and 406 nm were intensive, the MLCT peak could not be identified separately. For the same reason, MLCTs are not clear in the experimental UV-vis spectra. MLCT was also present at 389 nm, 381 nm, 379 nm, 306 nm, 304 nm and 302 nm with low oscillator strengths. The ligand was locally excited, having *n*–π* and π–π* transitions (LE3) at 308 nm, 310 nm and 325 nm.

Calculated total electron densities in DMF are displayed in Fig. S11. The electrostatic potential surface is used to obtain total electron densities. The lower and upper limits of the total electron density values for color coding are also given in Fig. S11. In all molecules, the positive electrostatic potential (blue area) is localized around the NH_2 in the bridge system. The C–S–C region has nearly negative charges. Pc also carries slightly negative charges.

NBO charges of the investigated molecules are given in Table S5. Total electron distribution indicated that electrons prefer to localize on phthalocyanine rings in DMF. These distributions show that C–S–C groups on bridges are slightly electron-accepting and electron-donating character and may be responsible for charge transfer between metal-phthalocyanine and diamino-pyrimidine bridges.

Adiabatic Ionization Potentials (AIP) and Vertical Ionization Potentials (VIP) were calculated using the transition from the neutral form to the cation. The energy difference between the neutral molecule (E_0) and its cation ($E.^*$) of the neutral molecule (VEA = $E.^* - E_0$) and between the neutral molecule and its cation in their most stable geometries (AEA = $E. - E_0$) were calculated, respectively (Table S6). VIP values were calculated as 5.55 eV, 5.76 eV and 5.54 eV, respectively. AIP values were also calculated as 5.49 eV, 5.67 eV and 5.49 eV, respectively. Close values calculated for VIP and AIP reveal that molecular geometries did not change significantly in neutral and cationic forms. Since **2** and **4** have lower ionization potentials than that of **3**, they could form the ionic structure more easily than **3**. Additionally, we calculated the hole reorganization energy (λ_h) of the molecules as 105 meV, 180 meV and 109 meV, respectively. Reorganization energy (λ_{outer} and λ_{inner}) is an important parameter that shows the intramolecular charge transfer rate for organic semiconductors [36, 37]. Low reorganization energy is related to high charge mobility of the system. Since the calculations are performed in gas phase and the molecules are not flexible, their outer reorganization energy is neglected. We calculated the inner reorganization energy which depends on the molecular geometry changes upon addition or removal of an electron from a molecule. We investigated donor characteristics of the molecules using hole reorganization energies and determined that they decrease in the order of **2** < **4** < **3**. With the lowest HOMO–LUMO gap, hole reorganization energy and lower ionization energy, **2** is the most suitable compound for OFET devices.

OFET studies

It is well known that interfaces present in device configuration are two determining factors for an OFET device [38]. At first, we aimed to investigate the gate dielectric-ITO interface *via* capacitance–frequency (C–f) and current–voltage (I–V) measurements, which are widely used methods for interface characterization. For this purpose, a device with Au/**2**–**4**/ITO structure was fabricated and characterized using C–f and J–V measurements at room temperature. The obtained J–V curves for all compounds are depicted in Fig. 8. A detailed evaluation of Fig. 8 indicates that the device with compound **2** exhibits the lowest leakage current density of < 6 nA cm^{-2} which is comparable with commercial polymeric dielectric materials [39, 40]. Highly non-linear behavior of the J–V curves under reverse and forward bias conditions is clear. In order to clarify the origin of the leakage current mechanism, experimental data were discussed in terms of Poole–Frenkel emission or Fowler–Nordheim tunneling [41, 42].

The Fowler–Nordheim tunneling model assumes that charge carriers are injected by means of quantum mechanical tunneling even with low energy. This model describes a relationship between the applied voltage and the observed current which can be defined as follows (Equation 1):

$$I = A\left(\frac{q^3}{8h\pi\varphi_{FN}}\right)\left(\frac{V}{d}\right)^2 \exp\left(-\frac{8d\pi\sqrt{2m^*}\sqrt[3]{\varphi_{FN}^2}}{3qVh}\right) \quad (1)$$

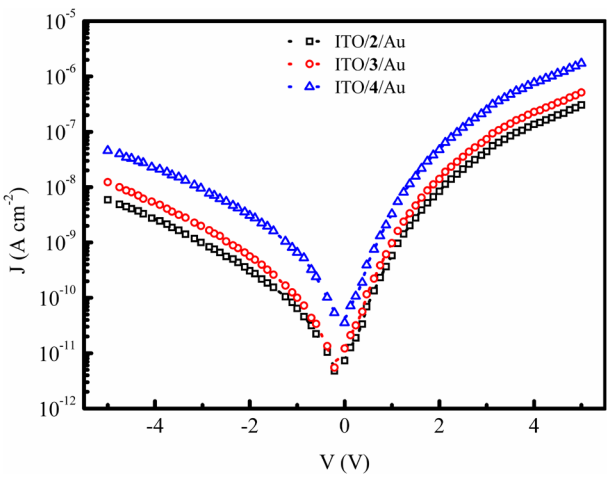

Fig. 8. J–V characteristics of the devices measured at room temperature

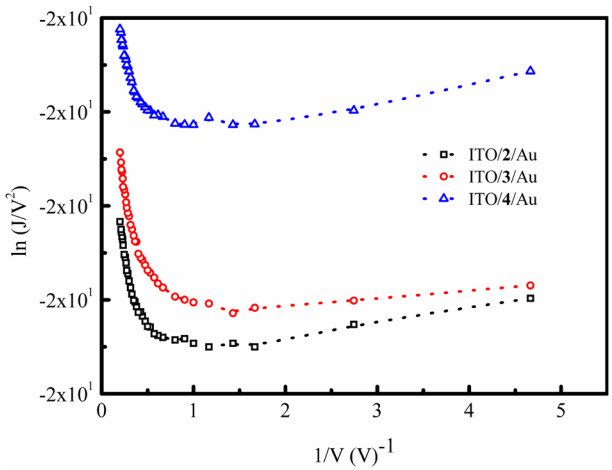

Fig. 9. Plots of experimental data according to Fowler–Nordheim tunneling model

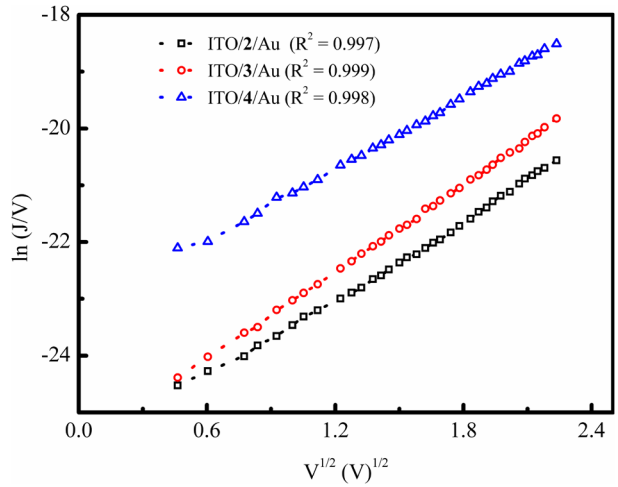

Fig. 10. Fitting of reverse bias J–V data to Poole–Frenkel effect

where A is the diode area, m^* is the effective mass, h is Planck's constant and φ_{FN} is the barrier height. Equation 1 reveals that, if the leakage current mechanism dominated by Fowler–Nordheim tunneling, the plot of $\ln(J/V^2)$ *vs.* $1/V$ should give a straight line with a constant slope. Fig. 9 shows the reverse bias $\ln(J/V^2)$ *vs.* $1/V$ plots for all compounds investigated. Deviations from linearity for the $\ln(J/V^2)$ *vs.* $1/V$ plots show that the observed leakage current mechanism cannot be treated using the concepts based on the Fowler–Nordheim tunneling model.

On the other hand, the Poole–Frenkel model assumes that the trapped charges at Coulombic traps are thermally activated for conduction with the help of an applied field. Additionally, the reaction $(E_c - E_v) >> kT$ should be satisfied by the difference between the conduction and valance band energies. Under these assumptions, the relation between the observed current and the applied voltage can be expressed as Equation 2 [43]:

$$I = A \frac{V}{d} \exp\left(\frac{q\varphi_{PF} - \beta_{PF}\sqrt{V/d}}{ckT}\right) \quad (2)$$

where A is a fitting parameter, $q\varphi_{PF}$ is the required energy for an electron to escape from the trap, c is the slope parameter and $\beta_{PF}\sqrt{V}$ is barrier lowering. According to Eq. 2, it can be concluded that if the leakage current originates from Poole–Frenkel emission, the slope of the ln (J/V) *vs.* $\sqrt{V}$ should be constant. In order to apply the Poole–Frenkel model to our experimental data, we presented ln (J/V) *vs.* $\sqrt{V}$ curves in Fig. 10 for all compounds. Correlation coefficients (R^2) confirmed the applicability of the Poole–Frenkel effect to reverse bias J–V data.

As shown in the inset of Fig. 10, high correlation coefficients between 0.997 and 0.999 reveal that the leakage current mechanism in ITO/**2–4**/Au devices is the Poole–Frenkel effect.

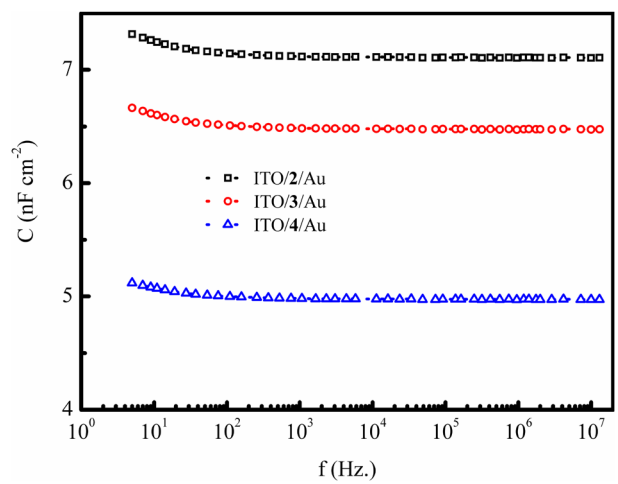

Fig. 11. Variation of the capacitance density with frequency for the ITO/**2–4**/Au structure

Frequency dependence of capacitance density, one of the most important performance parameters for gate dielectrics, was also investigated in a wide range of frequencies between 5 Hz and 13 MHz (Fig. 11). Frequency dispersion behavior for low frequencies and nearly frequency-independent behavior at high frequency region are clear. A capacitance density value of 9.3 nF/cm^2 at a frequency of 5 Hz and a slightly smaller value (9.02 nF/cm^2) at 13 MHz were obtained. The observed low-frequency dispersion reveals that molecular dipoles complete their alignment and contribute to the polarization. However, with increasing frequencies the dipoles cannot follow the variation in the frequency of the applied field.

Field-effect mobility (μ) is one of the most important parameters for an OFET. Recently, various models have been suggested and used to simulate the field-effect mobility in organic materials [44, 45]. However,

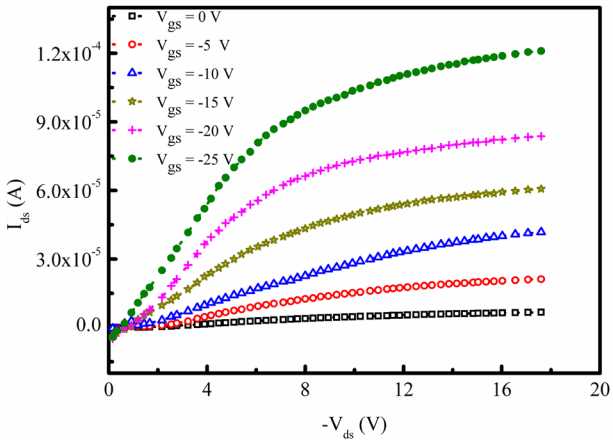

Fig. 12. Room temperature output characteristic of the pentacene-based OFET with **2** as gate dielectric

it has also been well-established that these models lack generalization [46]. In this work, field-effect mobility values were obtained from the measured output and transfer characteristics of the devices. In Fig. 12, we present output characteristics of the pentacene-based OFET device with compound **2** as gate dielectric for various values of gate-source voltage (V_{gs}). A linear increase in drain-source current (I_{ds}) with an increase of drain-source voltage (V_{ds}) can be seen for low V_{ds}. It is also clear that the drain source does not continue to increase linearly with further increases in V_{ds} voltage; rather, it exhibits saturation behavior for high V_{ds} voltages. Similar types of output characteristics were also obtained with **3** and **4** with different I_{ds} current values. The obtained output characteristics for **3** and **4** are presented in Figs S13 and S14, respectively. A reasonable explanation for the observed difference in drain current can be given as follows: it is demonstrated that the interaction between the gate insulator and the semiconductor material plays an important role in the operation of organic field-effect transistors [19]. The polarity of the dielectric interface can also influence the quality of the semiconductor layer by affecting local morphology and the density of states in the organic semiconductor layer. Combined experimental and theoretical analysis showed that the nature of the insulator interface has great impact on the performance of an OFET. It was concluded that the insulator is not only capable of affecting the morphology of the semiconductor layer, but can also change the density of states by local polarization effects. In this sense, several experimental and theoretical studies have shown that the difference in charge transport observed between organic semiconductors in OFETs is associated with the effects of disorder and interfacial traps [47]. Therefore, the observed differences in drain currents can be attributed to the differences in molecular structure, the solid state stacking arrangement of the molecules, and the metal–metal distance.

The observed linear dependence of I_{ds} current on for low V_{ds} values suggests that the dependence of the I_{ds} current on V_{ds} voltage can be formulated as Equation 3:

$$I_{ds} = \frac{W}{L} C_{ox} \mu \left(V_{gs} - V_{tr}\right) V_{ds} - \frac{1}{2} V_{ds}^2 \quad (3)$$

where W and L are the channel width and length, respectively; μ is the field-effect mobility for carriers, C_{in} is the insulator capacitance density and V_{tr} is the threshold voltage. For this region, the term v^2_{ds} in Equation 3 can be neglected and reduced to Equation 4.

$$I_{ds} = \frac{W}{L} C_{in} \mu (V_{gs} - V_{tr}) V_{ds} \quad (4)$$

On the other hand, the variation of the drain current with drain-source voltage can be represented by the following equation (5) for high values of V_{ds} voltage [48].

$$I_{ds} = \frac{W}{2L} C_{in} \mu \left(V_{gs} - V_{tr}\right)^2 \quad (5)$$

In this work, Equation 5 is utilized to describe I_{ds} in the saturation regime in order to calculate the field-effect mobility. For this purpose, transfer characteristics of the OFETs were measured for constant V_{ds} voltage and Eq. 5 was used to obtain the field effect mobility.

Fig. 13 shows those plots. According to Equation 5, the square roots of the I_{ds} current *vs*. V_{gs} plots should be linear in nature. With the aid of Equation 5, from the slope of the square roots of the I_{ds} *vs.* V_{gs} plots, field effect-mobilities of the devices were derived and found to be 4.7×10^{-2}, 3.3×10^{-2} and 1.7×10^{-2} $cm^2/(V \cdot s)$ for compounds **2**–**4**, respectively. Understanding the structural ordering at the dielectric–semiconductor interface is crucial for FET applications of organic semiconductors. On the other hand, it is well known that the polarity of the dielectric layer can influence the density of states in

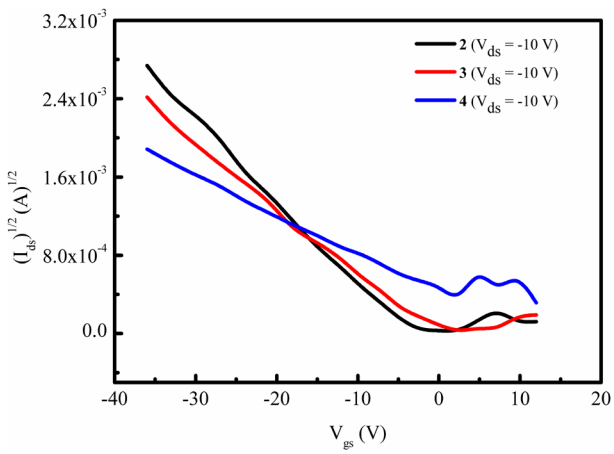

Fig. 13. Transfer characteristics of the OFET devices at indicated V_{ds} voltage

the organic semiconductor and consequently dominate the mobility of the devices. The observed trend for field-effect mobilities can be attributed to the magnitudes of the dipole moments of the compounds. This is consistent with the results of DFT calculations (Table S1).

CONCLUSION

In this work, we have synthesized and characterized three new ball-type phthalocyanines {M = Co (**2**), Zn (**3**), Lu (**4**)} with four 5,6-diaminopyrimidine substituents. DFT and TD-DFT calculations revealed that the phthalocyanine rings present in the studied molecules have distorted structures, deviating from planarity and lowering the symmetry of the Pcs. In compound **2**, Co(II) metals are close to each other, which results overlapping of Co(II)–Co(II) orbitals (dz^2) and may lead to the formation of Co(III) both in gas phase and in DMF, which has not been previously reported. The calculated UV-vis spectra of investigated molecules agree quite well with the experimental results. Comparing the HOMO–LUMO gaps and the reorganization energies, **2** has the smallest value among the examined compounds (**2** < **4** < **3**). According to the computational analysis, the decrease in the distance between the Pcs due to the *d–d* interaction resulted in an increase in π–π interaction and polarity, leading to an increase in OFET properties.

In order to investigate the performance of these compounds as gate dielectrics in OFET devices, OFETs were fabricated with a bottom-gate topcontact configuration. The leakage current mechanism in ITO/**2**–**4**/Au structures were also analyzed and discussed. Our studies clearly showed that the leakage current in ITO/**2**–**4**/Au structures is dominated by the Poole–Frenkel effect. Experimental and computational results have shown that compound **2** has great potential for use as a gate dielectric in bottom-gate top-contact OFET devices.

Acknowledgments

This work was supported by the Fırat University Scientific Research Project Coordination Unit, (FÜBAP), (Project No: FF.17.10), by Turkish Academy of Sciences, (TUBA) and by Yildiz Technical University, Scientific Research Project Foundation (Grant No: 2016-01-01-KAP04). Computer time provided on FenCluster by Faculty of Science, Ege University and on TUBITAK-ULAKBIM TRUBA resources are gratefully acknowledged.

Supporting information

Figures S1–S13 and Tables S1–S6 are given in the supplementary material. This material is available free of charge *via* the Internet at http://www.worldscinet.com/jpp/jpp.shtml.

REFERENCES

1. Leznoff CC and Lever ABP. (Eds.) *Phthalocyanines: Properties and Applications,* Vol. 1. VCH: Cambridge UK, 1993, 436 pp.
2. Schaumann E. (Ed.) *Methods of Organic Chemistry,* Huben-Weyl: Stuttgart, Germany, , 1998; **V.E9**: 717–846.
3. Bekaroğlu Ö. In *Structure and Bonding*, Mingos DM and Jiang J. (Eds.) 2010, Springer Verlag: Berlin, Heidelberg, pp. 105–135.
4. Salan Ü, Altındal A, Özkaya AR, Salih B and Bekaroğlu Ö. *Dalton Trans.* 2012; **41**: 5177–5187.
5. Bekaroğlu Ö. *Turk. J. Chem.* 2014; **38**: 903–922.
6. Özer LM, Özer M, Altındal A, Özkaya AR, Salih B and Bekaroğlu Ö. *Dalton Trans*. 2013; **42**: 6633–6644.
7. Kakı E, Altındal A, Salih B and Bekaroğlu Ö. *Dalton Trans.* 2015; **44**: 8293–8299.
8. Salan Ü, Kobayashi N and Bekaroğlu Ö. *Tetrahedron Lett.* 2009; **50**: 6775–6778.
9. Tolbin AY, Ivanov AV, Tomilova LG and Zefirov NS. *Mendeleev Commun.* 2002; **12**: 96–97.
10. Tolbin AY, Ivanov AV, Tomilova LG and Zefirov NS. *J. Porphyrins Phthalocyanines* 2003; **7**: 162–166.
11. Yazıcı A, Avcı A, Altındal A, Salih B and Bekaroğlu Ö. *J. Porphyrins Phthalocyanines* 2018; **22**: 149–156.
12. Altun S, Odabaş Z, Altındal A and Özkaya AR. *Dalton Trans*. 2014; **43**: 7987–7997.
13. Hong F, Guo X, Zhang H, Wei B, Zhang J and Wang J. *Organic Electronics* 2009; **10**: 1097–1101.
14. Mei J, Diao Y, Appleton AL, Fang L and Bao Z. *J. Am. Chem. Soc.* 2013; **135**: 6724–6746.
15. Ray AK. In *Springer Handbook of Electronic and Photonic Materials Organic Materials for Chemical Sensing*, Kasap S and Capper P. (Eds.) 2017, Springer Handbooks, Springer: New York, pp. 1281–1310.
16. Doğan E, Özer M, Altındal A, Özkaya AR, Salih B and Bekaroglu Ö. *J. Porphyrins Phthalocyanines* 2016; **20**: 1319–1333.
17. Nwaji N, Oluwole DO, Mack J, Louzada M, Khene S, Britton J and Nyokong T. *Dyes Pigm.* 2017; **140**: 417–430.
18. Nwaji N, Mack J and Nyokong T. *Opt. Mater.* 2018; **82**: 93–103.
19. Ortiz RP, Marks A and Facchetti TL. *Chem. Rev.* 2010; **110**: 205–239.
20. Unni KNN, Dabos-Seignon S, Pandey AK and Nunzi J-M. *Solid-State Electron.* 2008; **52**: 179–181.
21. Pyo S, Son H, Choi K, Yi M and Hong S. *Appl. Phys. Lett*. 2005; **86**: 133508-1–133508-3.
22. Uemura S, Yoshida M, Hoshino S, Kodzasa T, Kamata T. *Thin Solid Films* 2003; **438**: 378–381.
23. Çelikbıçak Ö, Demirel G, Pişkin E and Salih B. *Anal Chim Acta.* 2012; **729**: 54–61.

24. Şengül A, Doğan HZ, Altındal A, Özkaya AR, Salih B and Bekaroğlu Ö. *Dalton Trans.* 2012; **41**: 7559–7572
25. Frisch MJ, Trucks GW, Schlegel HB, Scuseria GE, Robb MA, Cheeseman JR, Scalmani G, Barone V, Mennucci B, Petersson GA, Nakatsuji H, Caricato M, Li X, Hratchian HP, Izmaylov AF, Bloino J, Zheng G, Sonnenberg JL, Hada M, Ehara M, Toyota K, Fukuda R, Hasegawa J, Ishida M, Nakajima T, Honda Y, Kitao O, Nakai H, Vreven T, Montgomery, Jr. JA, Peralta JE, Ogliaro F, Bearpark M, Heyd JJ, Brothers E, Kudin KN, Staroverov VN, Kobayashi R, Normand J, Raghavachari K, Rendell A, Burant JC, Iyengar SS, Tomasi J, Cossi M, Rega N, Millam JM, Klene M, Knox JE, Cross JB, Bakken V, Adamo C, Jaramillo J, Gomperts R, Stratmann RE, Yazyev O, Austin AJ, Cammi R, Pomelli C, Ochterski JW, Martin RL, Morokuma K, Zakrzewski VG, Voth GA, Salvador P, Dannenberg JJ, Dapprich S, Daniels AD, Farkas Ö, Foresman JB, Ortiz JV, Cioslowski J and Fox DJ. Gaussian, Inc., Gaussian 09, Revision C.01, Wallingford, CT, 2009.
26. Dennington R, Keith T and Millam J. GausView 5.0.9, Semichem Inc., Shawnee Mission KS, 2009.
27. Kohn W and Sham LJ. *Phys Rev.* 1945; **140**: A1133–A1138.
28. Becke AD. *Phys. Rev. A* 1988; **38**: 3098–3100.
29. Becke AD. *J. Chem. Phys.* 1993; **98**: 5648–5652.
30. Lee C, Yang W and Parr PG. *Phys. Rev. B* 1988; **37**: 785–789.
31. Yanai Y, Tew D and Handy N. *Chem. Phys. Lett*. 2004; **393**: 51–57.
32. Dunning TH Jr and Hay PJ. In *Mod. Theor. Chem*. Schaefer III HF. (Ed.) Vol. 3, 1977, Plenum: New York, pp. 1–28.
33. Tomasi J, Mennucci B and Cancès E. *J. Mol. Struct. THEOCHEM* 1999; **464**: 211–226.
34. Tomasi J, Mennucci B and Cammi R. *Chem. Rev.* 2005; **105**: 2999–3094.
35. Glendening ED, Reed AE, Carpenter and Weinhold F. *NBO* (Natural Bond Orbital) program, Version 3.1.
36. Marcus RA. *J. Chem. Phys*. 1956; **24**: 966–978.
37. Ran XQ, Feng JK, Ren AM, Li WC, Zou LY and Sun LL. *J. Phys. Chem*. 2009; **A113**: 7933–7939.
38. Di C-A, Liu Y, Yu G and Zhu D. *Acc. Chem. Res*. 2009; **42**: 1573–1583.
39. Lee SH, Choo DJ, Han SH, Kim JH, Son YR and Jang J. *Appl. Phys. Lett*. 2007; **90**: 033502.
40. Yoon M-H, Yan H, Facchetti A and Marks TJ. *J. Am. Chem. Soc.* 2005; **127**: 10388–10395.
41. Chaneliere C, Autran JL, Devine RAB and Balland B. *Mater. Sci. Eng.* 1998; **R22**: 269–322.
42. Fowler RH and Nordheim L. *Proc. R. Soc. London* 1928; **119**: 173–181.
43. Harrell WR. Poole–Frenkel Conduction in Silicon Dioxide Films, and Implications for Hot-Carrier Degradation in *n*-MOS Devices, Doctoral Dissertation, University of Maryland, 1994.
44. Yan H, Yoon MH, Facchetti A and Marks TJ. *Appl. Phys. Lett.* 2005; **87**: 183501.
45. Wang J, Yan X, Xu Y, Zhang J and Yan D. *Appl. Phys. Lett.* 2004; **85**: 5424–5426.
46. Guo W, Shen L and Ma D. *Optik* 2009; **120**: 668–672.
47. Veres J, Ogier SD, Leeming SW, Cupertino DC and Khaffaf SM. *Adv. Funct. Mater.* 2003; **13**: 199–204.
48. Sze SM and Ng KK. *Physics of Semiconductor Devices*. John Wiley & Sons, Inc: Hoboken, NJ, 2006.